DEUTSCHES ELEKTRONEN-SYNCHROTRON DESY

DESY SR-79/23
October 1979

EXPERIMENTAL SETUP FOR X-RAY ABSORPTION SPECTROSCOPY AT THE DESY

by

P. Rabe, G. Tolkiehn, A. Werner
Institut für Experimentalphysik der Univereität Kiel

Eigentum der DESY Bibliothek
Property of library
Zugang: 22. OKT. 1979
Accession:
Leihfrist: 7 Tage
Loan period: days

NOTKESTRASSE 85 · 2 HAMBURG 52

To be sure that your preprints are promptly included in the
HIGH ENERGY PHYSICS INDEX ,
send them to the following address (if possible by air mail) :

DESY
Bibliothek
Notkestrasse 85
2 Hamburg 52
Germany

DESY SR-79/25
October 1979

"Experimental Setup for X-Ray Absorption Spectroscopy at the DESY"

P. Rabe, G. Tolkiehn, A. Werner
Institut für Experimentalphysik Universität Kiel,
Kiel, Germany

Abstract

In this paper we describe an apparatus used at the Deutsches Elektronen-Synchrotron (DESY) for the measurement of x-ray absorption spectra, specially designed for the investigation of the extended x-ray absorption fine structure (EXAFS). Performance of the setup is discussed and compared with an apparatus using the bremsstrahlung of a conventional x-ray source.

1. Introduction

The EXAFS has been known to appear in the x-ray absorption spectra of practically all materials[1]. It offers a powerful new method for the determination of the local geometrical structure around specific atoms[2]. The relatively small amplitudes of the EXAFS on a high absorption background as demonstrated in Fig. 1 require high accuracy absorption spectra over a wide energy range (up to more than 1 keV) to get reliable structure data. Therefore, the EXAFS method has developped rapidly since synchrotrons and storage rings became available as intense continuous x-ray sources.

At DESY a horizontal angle of 1mrad of synchrotron radiation is available which gives the spectral intensity distribution shown in Fig. 2 in comparison with the bremsstrahlung intensity of a 12 kW rotating anode x-ray generator. The white beam is monochromatized by double Bragg reflection in parallel setting[3]. The "channel-cut" single crystals of Ge and Si are cut parallel to 111 and 220 net planes respectively. By rotating these crystals in principle the photon energy can be tuned over the range of 2.5 keV to 28 keV. As the monochromator works in air, the spectral range is limited to energies above ∿5 keV. As the monochromatic light is plane-polarized to >90 %, polarization effects in absorption spectra can be investigated over the whole energy range[4].

A schematic view of the whole setup is given in Fig. 3. Detectors, slits and sample chamber are mounted on a step-motor driven table.

The table follows the parallel shift of the monochromatic beam as the monochromator crystal is rotated. The channel widths of the Ge and Si crystals are 10 mm and 4 mm, so the maximum range of parallel shift is 20 mm and 8 mm respectively. The step-motors of the goniometer with the crystal and of the table are controlled by a small computer (PDP8/e) which also accumulates the data. The detectors are ionization chambers. The ionization currents are amplified and converted to frequencies by 100 kHz voltage- to - frequency converters.

Both signals from in front of (reference) and behind (signal) the sample are counted until a preset value in the reference scaler is reached, thus dividing signal by reference instantly After readout, the goniometer is set to the next angle, and both counters are started again. In this way spectra of up to 900 data points can be taken. The typical scan rate is ≈1 point/s. The minimum rotation angle of the goniometer is 0.001 degrees. The spectra can be stored on DEC-tape for later interactive evaluation on a large IBM computer via a second PDP 8/e.

2. Light source geometry

In order to characterize and optimize the x-ray optics involved, the synchrotron light source can conveniently be described in terms of a phase space representation[5]. The coordinate system used therefore is shown in Fig. 4. At z = 0, the e^- beam moves in z-direction. Every electron or photon passing through the source plane (z=0-plane) is presented by a set of four coordinates, namely horizontal and

vertical spatial (x, y) and angular (x', y') coordinates (cf. ref. 5). The time-averaged electron-distribution $I_\perp$ in the vertical coordinates y, y' can be assumed to be Gaussian:

$$I_\perp(y, y') \propto \exp\left\{-\left(\frac{y^2}{{y_o}^2} + \frac{\left(y' - \frac{\alpha}{\beta}y\right)^2}{\left(\frac{y_o}{\beta}\right)^2}\right)\ln 2\right\} \qquad (1)$$

where α, β are the electron optical parameters (α=0, β=20.925 m at DESY) and $2y_o$ is the fwhm of the electron beam (2 mm at DESY). The half-maximum line of eq. 1 is an ellipse with the parametrized representation (Fig. 5, dashed line):

$$y = y_o \cos\psi$$
$$y' = \frac{y_o}{\beta}(\sin\psi + \alpha\cos\psi) \qquad (2)$$

Every electron emits photons into a cone whose width depends on the electron and photon energies[6].

So the angular component of the intensity distribution has to be convoluted with the photon angular distribution. If the photon angular distribution is a Gaussian with half width s = 0.075 mrad (time average calculated for the DESY at 7,2 GeV max. electron energy and 13,5 keV photon energy), the half width of the angular part of eq.1 y_o/β = 0.048 mrad is broadened to

$$\frac{y_o}{\beta'} = \sqrt{s^2 + (y_o/\beta)^2} = 0.089 \text{ mrad}$$

The photons' half intensity ellipse eq. 2 is then given by the new values

$$\beta' = \left(\frac{s^2}{{y_o}^2} + \frac{1}{\beta^2}\right)^{-1/2} = 11.24 \text{ m and } \alpha' = \beta'\frac{\alpha}{\beta} = 0$$

(cf. Fig. 5 solid line).

To show its effect on the photon beam, in Fig. 5 an exit slit of vertical width d_y = 2 mm at z = 37 m is projected back to z = 0 by

$y(0) = y(z) - zy'$. The hatched area in Fig. 5 represents the main part of the photon flux that can pass through this slit.

The angular half-width (divergence) of the beam behind the exit slit was calculated by integrating eq. 1 over y, for different slit widths. The result is shown in Fig. 6 (full circles). Integrating additionally over y' gives the total photon flux vs. slit width (Fig. 6 open circles). The horizontal bar indicates the region of d_y in which the slit can be used effectively for reducing the divergence of the beam. Of course, also photons emitted at $z \neq 0$, whose intensity distribution in vertical phase space is slightly different when projected to $z = 0$, can enter the monochromator. But as the "visible" z-range is rather short (ca. 25 cm) due to the horizontal curvature of the electron orbit (v.i.), this small distortion is neglected here. Additionally, Fig. 6 shows the degree of polarization P (crosses) which is defined as

$$P = \frac{I_{\parallel} - I_{\perp}}{I_{\parallel} + I_{\perp}}$$

where $I_{\parallel}$ and $I_{\perp}$ are the horizontal and vertical polarization components integrated over the slit width d.

In the horizontal direction the phase space representation of the e^- beam at $z = 0$ yields a larger e^- ellipse (Fig. 7, solid line). The photon broadening is neglected here as it is in the range of the line widths in Fig. 7. Additionally, due to the curvature of the beam with radius R = 31.7 m, the phase space representation of the photon flux is actually a superposition of distributions centered at $x = -R(1-\cos x')$. This leads to an intensity distribution with half-maximum lines at $x = \pm x_0 - R(1-\cos x')$ (Fig. 7, dot-dashed lines). The synchrotron is therefore nearly an isotropic source in the horizontal direction.

The projection to $z = 0$ of a slit of horizontal width $d_x = 30$ mm as used in our experiments is shown in Fig. 7. An angular half intensity width (horizontal divergence) of 0.88 mrad behind the slit is calculated by integration of the horizontal analogue of eq. 1 over x. The ellipse centered at $x' = 4$ mrad, $x = -0.2$ mm shown in Fig. 7 (dashed line) is the representation of the source at $z = -12.6$ cm. This illustrates that only a small fraction of radiation from electrons with $-12{,}5 \text{ cm} > z > 12{,}5$ cm passes the slit.

3. Energy resolution of the monochromator

The monochromator is placed at a distance of 37 m from the source point in the synchrotron. A horizontal axis of rotation for the crystals in nondispersive setting has been chosen because of the smaller effective divergence in the vertical direction and the high degree of horizontal polarization.

The energy width ΔE transmitted in first order Bragg reflection depends on the following three values:

1. The $\frac{\Delta\lambda}{\lambda}$ of the crystal due to the diffraction pattern.
2. The vertical divergence of the light $\Delta\psi_y$.
3. The horizontal divergence $\Delta\psi_x$.

The total transmitted energy band width (fwhm) ΔE can be approximated as the quadratic sum of the three corresponding widths given in approximate form for small $\Delta\psi_x$, $\Delta\psi_y$ and $\theta_B < 60^\circ$:

$$\Delta E = E\sqrt{\left(\frac{\Delta\lambda}{\lambda}\right)^2 + \left(\Delta\psi_y \cot\theta_B\right)^2 + \left(\frac{1}{2}\Delta\psi_x^2\right)^2} \qquad (3)$$

where $E = \frac{hc}{2D \sin\vartheta_B}$ is the mean transmitted photon energy at the mean glancing angle ϑ_B and D is the spacing of the net planes. The third, horizontal divergence term is negligible in our case as $\Delta\psi_x \approx 1$ mrad The first (dashed line) and second (dotted line) components and their quadratic sum (solid line) are shown in Fig. 8 for Si 220 and Ge 111 As can be seen, only the 2 mm vertical slit results in a sufficient energy resolution in the range beyond 20 KeV. The energy resolution has not been measured directly, but the white line in K_2CrO_4 (Fig. 9) at 5989 eV in our absorption spectra has a half width of 2.4 eV where eq. 3 yields a resolution of 2.1 eV for the Ge 111 crystal.

4. Detectors

Photon counting is not feasible because monochromatic photon fluxes of more than 10^8/s can occur and additionally the photon flux has an adverse time structure. The x-ray photons are emitted in about 5×10^5 pulses during about 1 msec with a dark period of 19 ms, that is, each pulse of ≈100 ps contains ≈ 10 photons. Therefore, the detectors are ionisation chambers (IC) with 10 µm thick Kapton windows.

The planar copper electrodes of the IC's have a spacing of 10 mm and a voltage of 10^3 V between them. The gap can be filled with air, N_2, Ar, Kr, Xe in a pressure range of ≈ 0.1 b to 1b depending on the energy range of the absorption measurement. In order to get the same diffusion times of the ions in both of the chambers (cf. Section 7), the same gas and the same pressure in signal and reference IC are used. The signal which one gets as $S = \ln \frac{I_{ref}}{I_{sig}}$, where I_{ref} and I_{sig} are the currents of the reference and signal IC's, then contains a component depending on the energy dependence of the absorption of the chambers:

$$S = \mu(E)d + \ln\left(\frac{\exp(\mu_I(E)\cdot d_R) - 1}{1 - \exp(-\mu_I(E)\cdot d_S)}\right) \qquad (4)$$

Here $\mu(E)$ is the absorption coefficient of the sample with thickness d and $\mu_I(E)$ is the absorption coefficient of the reference and signal IC with lengths d_R and d_S, respectively.

5. Samples

Solid and liquid samples have been investigated with the equipment described above. Due to the exit slit size the samples have a typical area of 3 x 30 mm^2. They are mounted on a cooling/heating device in a vacuum chamber and measurements can be performed from LNT to ≈600 K. In order to get optimum signal to noise ratio (cf. ch. 7) the sample thickness should be chosen in a way that the transmission in the EXAFS region is about 10%. This corresponds to a thickness of several µm. The liquid samples are prepared between thin mylar foils and the thickness can be adjusted after preparation.

Beside the average thickness the second important feature of the sample is the homogeneity of the thickness. Pinholes, bubbles or any kind of variation in the sample thickness or composition over the irradiated area lead to an apparent decrease of the EXAFS amplitude.

If a certain fraction R of the sample area consists of holes, while the rest has homogeneous thickness d, then it is straightforward to calculate the measured signal S for a given absorption edge height $\Delta\mu$ and for a small variation $\delta\mu$(EXAFS) in μ. The quantities $\delta\mu/\Delta\mu$ and $\delta S/\Delta S$ are

proportional to the actual and the measured EXAFS amplitude χ and χ_m respectively. In Fig. 10 we have plotted χ_m/χ vs. R for different values of $\mu \cdot d$. It is obvious that for thick samples even small inhomogeneity causes drastic amplitude reductions. This does not affect the periodicity of the EXAFS from which bond lengths are evaluated[8]. If only bond lengths are to be determined, one can e.g. simply use powderized samples. But as soon as the amplitude of the EXAFS is involved, e.g. to determine coordination numbers or Debye-Waller factors, more sophisticated preparation techniques are necessary. The amplitude of the EXAFS can also be influenced by scattered radiation and higher order Bragg reflexes. Therefore, shielding against scattered radiation and suppression of higher orders are important (cf. ch. 8).

6. Intensity of the photon beam

The photon flux of the monochromatic x-rays can be estimated in two ways:

1. From the intensity distribution of the synchrotron radiation in phase space, taking into account absorption losses in the Be-window (1.5 mm) and in the air (40 cm), and including the action of the crystal, for Ge 111 we calculate a monochromatic flux of $\Phi_1 = 3 \cdot 10^9$/s at E = 7 keV photon energy, 8 mA electron current in the DESY operating at 7.2 GeV maximum energy.

2. From the measured ionization current $I_i = 3 \cdot 10^{-9}$ A at the same parameters we get with an average ionization energy of $E_i = 34$ eV per ion pair [9] in the air filled IC with $d_R = 10$ cm the photon flux:

$$\Phi_2 = \frac{I_i \cdot E_i}{2e \cdot E \cdot \exp.(-\mu d_R)} = 8.5 \times 10^8/s$$

Both of these values may well be wrong by a factor of 2, so the agreement is reasonable. Similar considerations for a 12 kW rotating anode x-ray generator with an Ag anode and a flat LiF crystal monochromator[8] at 10 keV with $\sim$ 5 eV resolution yield a flux of $3 \cdot 10^5$/s. With curved crystal monochromators, however, this figure may be increased by orders of magnitude without too much damaging the resolution[10]. Here problems arise from the appearance of characteristic lines in the spectra. In contrast the synchrotron radiation exhibits a structureless spectrum over a large spectral range. At certain energies, however, spikes in the absorption spectra may occur, which have nothing to do with the absorption coefficient of the sample or the source characteristics (see insert of Fig. 1). At these energies, the transmission of the monochromator is reduced by up to 50%. This effect is seen whenever additional to the ordinary Bragg reflex another outgoing wave into a different direction with the same wavelength is possible. Due to dynamic diffraction the different Bragg orders have different rocking curves. Therefore, the ratio of first order to higher order intensity may change strongly near such points. This leads to a spike in the absorption spectrum, because the first order is absorbed stronger than the higher orders. Of course, also any constant background, such as scattered x-rays or fluorescence enhances the height of the spike.

7. Signal to noise ratio

A numerical calculation minimizing the ratio of the mean square displacement of a data point measured in one second due to photon statistics to a small variation $\Delta\mu d$ in the absorption spectrum yields the optimum transmission of the sample ($\approx$ 10%) and the ionization chambers. Assuming $5 \cdot 10^8$ photons/s incident on the first detector one obtains a value of $1.1 \cdot 10^4$ for signal to noise ratio. Actually, a signal to noise ratio of $0.2 \cdot 10^4$ has been measured. This is mainly due to the time structure of the radiation (cf.section 4). The "duty cycle" of the radiation pulses is 1/20. So the average output voltage of the current amplifiers has to be lower than the maximum output voltage by at least this factor 20. This leads to a signal-to-noise ratio generated only by the current amplifier alone of already less than $5 \cdot 10^3$. Additionally, the beam-intensity fluctuates strongly from one pulse to the next one (up to $\pm$ 100%). So any difference between signal and reference channel in any of the time constants involved, even for very large ones, results in additional noise on the divided signal as a response to the intensity fluctuation. These are special problems, due to the time structure of a synchrotron which do not occur at storage rings or x-ray tubes.

8. Higher order Bragg reflections

Photons of higher order Bragg reflections usually yield a monotonous background in the transmission spectra that influences the amplitude

of the EXAFS signal in the same way as inhomogeneities in the sample. Additional structure can occur if there are absorption edges at the n-fold energy. The intensity of the nth order signal is, however, much lower than the first order signal for the following reasons:

1. The integrated intensity of the higher order light is proportional to the width of the diffraction pattern of the crystal which is proportional to $1/n^2$ (n is the order of the reflexion).

2. The intensity is proportional to the atomic form factor which decreases with increasing energy and to the structure factor which may be zero for specific orders, e.g. for second order of Ge and Si in all odd indexed net planes such as 111, 311, etc.

3. The intensity of the SR drops with increasing energy (cf. Fig. 2). This is only partly compensated by the decreasing absorption of the air.

4. The efficiency of the detectors decreases with increasing energy, the efficiency ε being the ionisation current per incident photon:

$$\varepsilon \propto E \cdot (1 - e^{-\mu(E) \cdot d_s})$$

where E is the photon energy and $\mu(E) \propto E^{-3}$ not too close to the absorption edges. For the signal chamber with 84% absorption in first order (optimum value) the energy being one, it is 0.49 for

second, 0.24 for third, 0.135 for fourth, if no absorption edges are present in the gas in this energy range.

This means for instance that for Ge III at 10 keV first order energy the ionisation current of the third order should be smaller by a factor of 0.002 for all gases. If in this case a sample with $\mu \cdot d \approx 2$ for first order is measured, which has practically no absorption at 30 keV, the ratio of third order signal to first order signal should be 0.02. This is equivalent to a fraction R =0.2% of holes in the sample which leads to a decrease of the EXAFS amplitude of no more than 1%. Such effects were not investigated systematically. However, for thick samples ($\mu d \geq 4$) they were seen to be prohibitive.

9. Summary

A device has been built up to take advantage of the high intensity x-radiation of the DESY for measuring the EXAFS. Within 15 min, 10^3 data points with about a factor of 10 better signal to noise ratio, a factor 150 shorter run time and a factor of 2 better in energy resolution can be measured compared to a 12 kW rotating anode x-ray generator. The apparatus has been successfully used for a number of experiments. It offers the advantage of strongly polarized radiation which makes also direction dependent structure analyzing by EXAFS possible. Due to the high energy resolution the instrument may also be used for near-edge-structure investigations.

Acknowledgements

We would like to thank Dr. N. Schwentner for helpful discussions. The support of Prof. R. Haensel is gratefully acknowledged. This work was financially supported by the Bundesministerium für Forschung und Technologie BMBF.

References

1 L.V. Azaroff and D.M. Pease in X-Ray Spectroscopy, ed. L.V. Azaroff (McGraw Hill, New York 1974), p. 284

2 E.A. Stern, Phys. Rev. B 10 (1974); 3027

F.W. Lytle, D.E. Sayers and E.A. Stern, Phys. Rev. B 11 (1975); 4825

E.A. Stern, D.E. Sayers and F.W. Lytle, Phys. Rev. B 11 (1975); 4836

3 J.H. Beaumont and M. Hart, J. Phys. E 7 (1974); 823

4 P. Rabe, G. Tolkiehn and A. Werner, Z. Krist. 149 (1979); 182

5 P. Pianetta and I. Lindau, Nucl. Instrum. and Meth. 152 (1978); 155; J. Elec. Spectr. & Rel. Phen. 11 (1977); 13

J.B. Hastings, B.M. Kincaid and R. Eisenberger, Nucl. Instrum. & Meth. 152 (1978); 167

6 C. Kunz in Synchrotron Radiation, ed. C. Kunz (Springer-Verlag, Berlin, 1979)

7 P. Rabe, G. Tolkiehn and A. Werner, J. Phys. C 12 (1979); 1173
J. Phys. C 12 (1979); 899; Jap. J. Appl. Phys. 17-2 (1978); 215

G. Martens, P. Rabe, G. Tolkiehn and A. Werner, phys. stat. sol. 55 (1979)

P. Rabe, Jap. J. Appl. Phys. 17-2 (1978); 22

8 G. Martens, P. Rabe, N. Schwentner and A. Werner, Phys. Rev. B 17 (1978); 1481

9 Dearnaley and Northrop, Semiconductor Counters for Nuclear Radiation, 2nd edition (E.+ F.N. Spon Ltd., London 1966) p. 21

10 J.A. del Cueto and N.J. Shevchik, J. Phys. E 11 (1978); 616

Figure Captions

Fig. 1 Absorption of IrO_2 at 77 K at the Ir L_{III}-edge.

Fig. 2 Calculated photon flux of DESY through a 30 mm wide, 8 mm high window at z = 40 m from the source point vs. photon energy, for different maximum energies compared to the flux of an x-ray generator into the same solid angle.

Fig. 3 Schematic diagram of the experimental setup.

Fig. 4 Definition of the coordinate system for phase space representation. The origin (source point) lies on the equilibrium electron orbit at its tangent point with the center of the beam pipe.

Fig. 5 Representation in phase space of the vertical component of electron (dashed) and 13,5 keV x-ray beam (solid ellipse) half-width line. The hatched area between the straight lines is transmitted through the 2 mm slit at z = 37 m.

Fig. 6 Calculated values for: a) vertical angular width $\Delta y'$ (fwhm) of the x-ray beam (13,5 keV) and b) the corresponding x-ray flux and c) degree of polarization behind slit at z = 37 m with vertical width d at 7,2 GeV electron energy and 10 keV photon energy.

Fig. 7 Horizontal phase space component of x-ray beam. Solid ellipse at z = 0, dashed ellipse at z = -12,5 cm. The hatched area between the straight lines is transmitted through the 30 mm slit at z = 37 m. The dot-dashed lines are the half-width lines of the superposition of the ellipses at all z values.

Fig. 8 Components and their quadratic sum (solid lines) of the energy resolution due to the rocking curve width of the crystal (dashed lines) and due to the vertical divergence $\Delta y'$ of the beam (dotted lines) versus transmitted energy for Ge 111 and Si 220.

Fig. 9 Absorption spectrum of K_2CrO_4 at the Cr K-edge.

Fig. 10 Ratio of measured to actual amplitude of $\chi(k)$ vs. inhomogeneity of the sample thickness in terms of the percentage R of the sample area covered by holes. Calculated for different sample thicknesses $\mu \cdot d$ for $E > E_{edge}$ and a ratio of $\mu(E < E_{edge}) / \mu (E > E_{edge}) = 0.135$ corresponding e.g. to the K-edge of metallic copper.

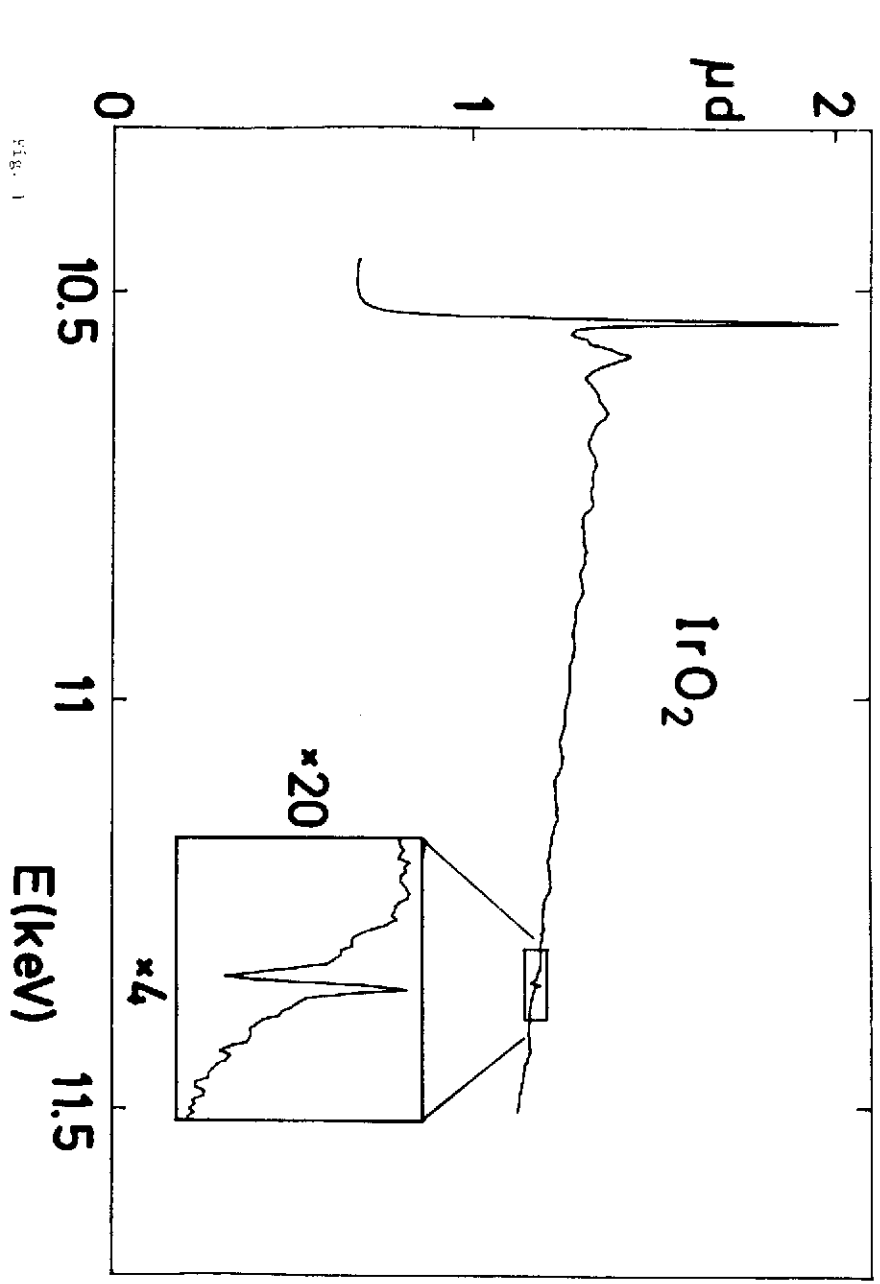
0
1
2
μd
10.5
11
11.5
E(keV)
IrO2
×20
×4

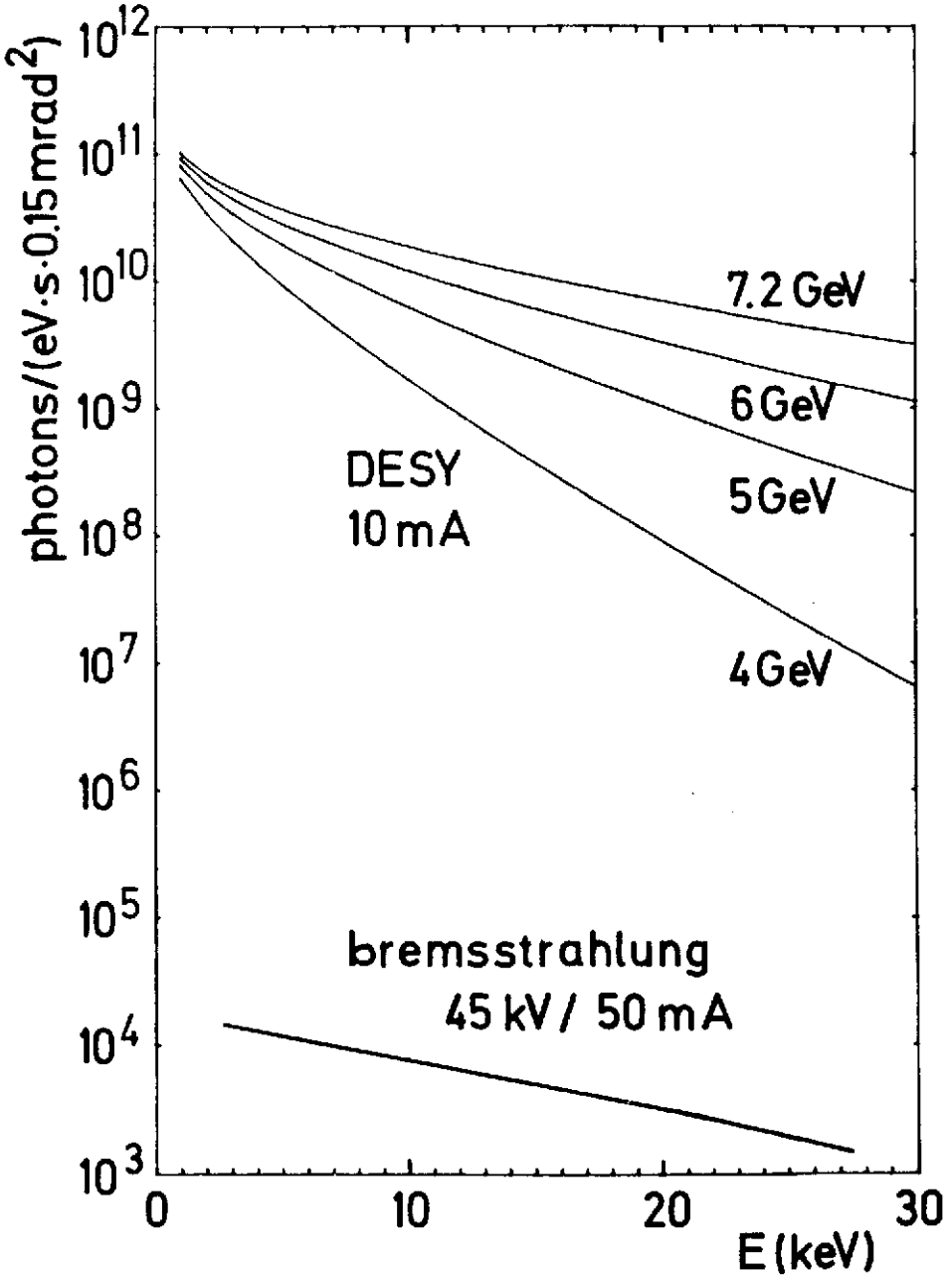
photons/(eV·s·0.15mrad²)
10¹²
10¹¹
10¹⁰
10⁹
10⁸
10⁷
10⁶
10⁵
10⁴
10³
7.2 GeV
6 GeV
5 GeV
4 GeV
DESY
10 mA
bremsstrahlung
45 kV / 50 mA
0
10
20
30
E (keV)

Fig. 2.

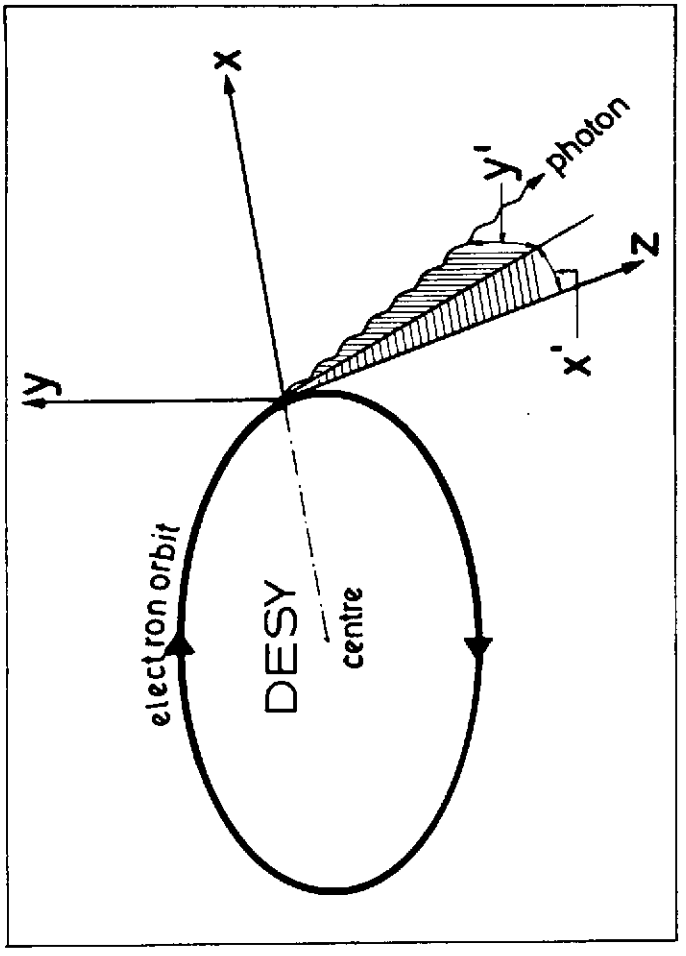
x
y'
photon
z
x'
y
electron orbit
DESY
centre

Fig. 4

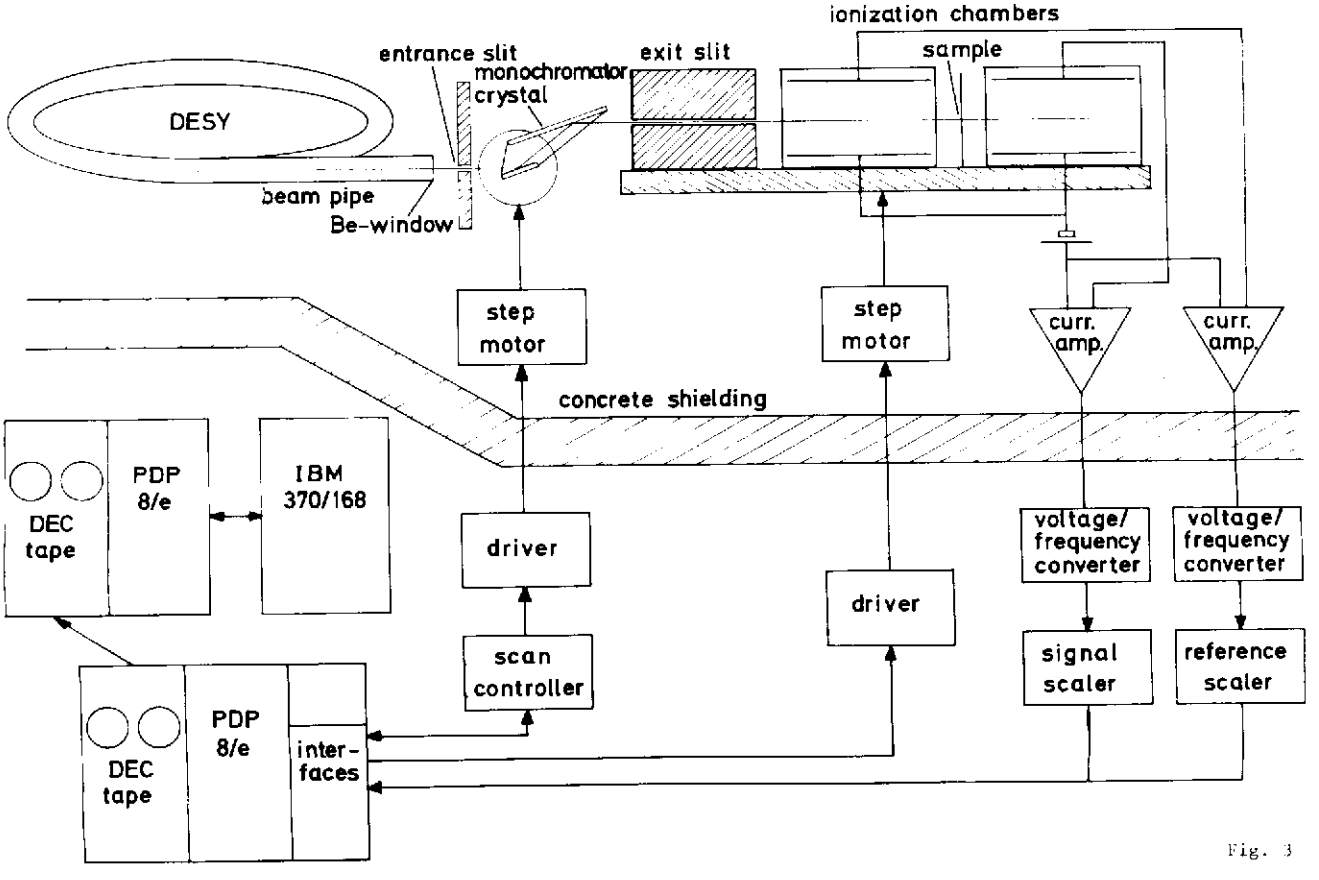
ionization chambers
entrance slit
monochromator crystal
exit slit
sample
DESY
beam pipe
Be-window
step motor
step motor
curr. amp.
curr. amp.
concrete shielding
PDP 8/e
DEC tape
IBM 370/168
driver
driver
voltage/ frequency converter
voltage/ frequency converter
scan controller
signal scaler
reference scaler
PDP 8/e
DEC tape
inter-faces

Fig. 3

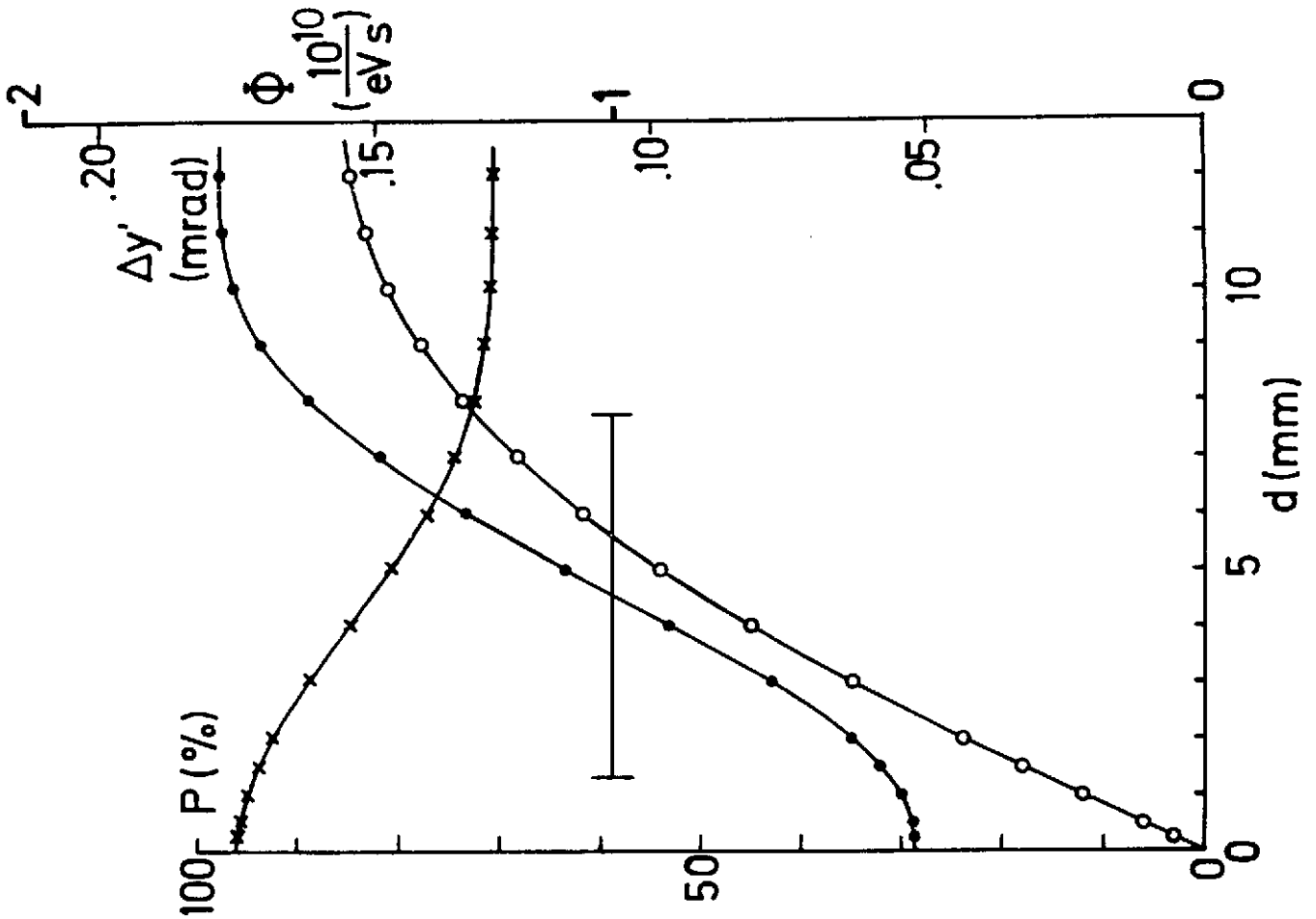
Φ $\frac{10^{10}}{(eVs)}$
2
1
0
.20
.15
.10
.05
Δy' (mrad)
P (%)
100
50
0
0
5
10
d(mm)

Fig. 6

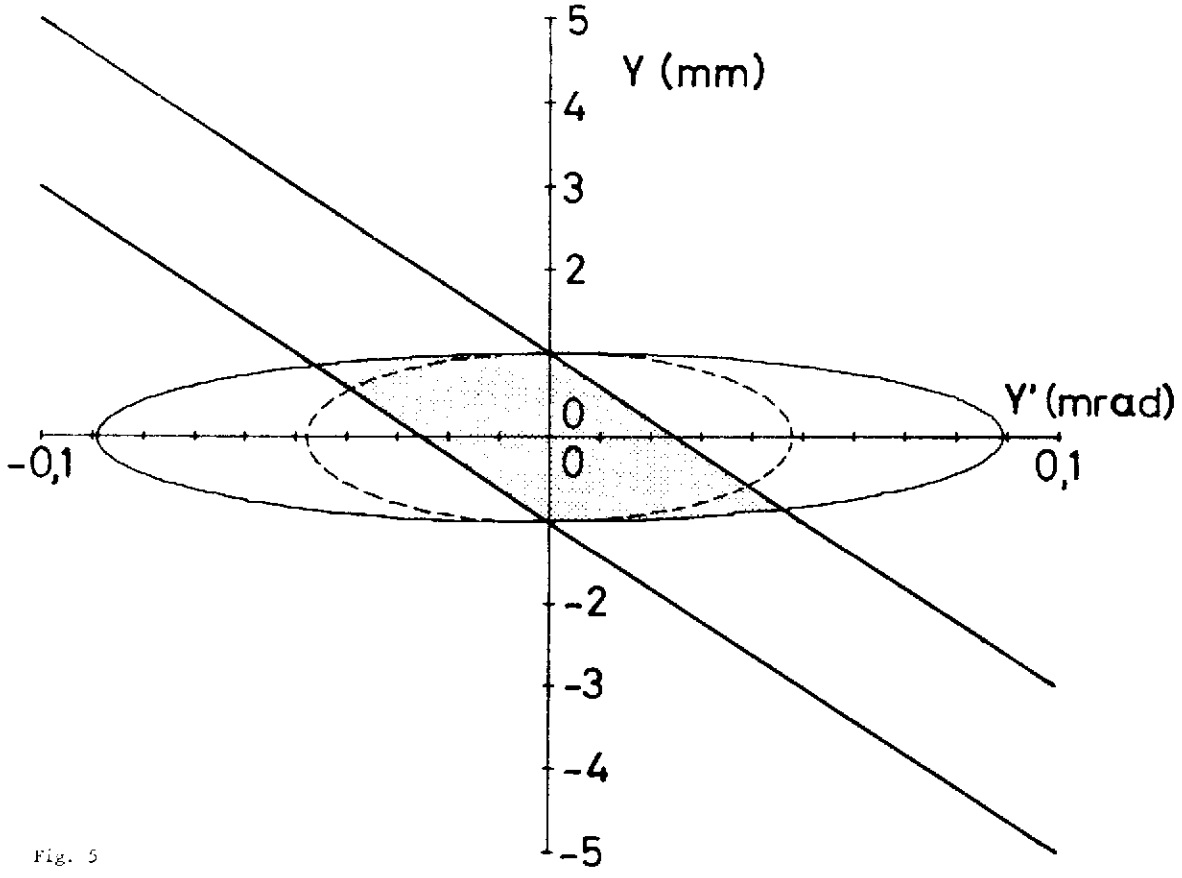
Y (mm)
5
4
3
2
0
-2
-3
-4
-5
Y' (mrad)
-0,1
0,1
0
0

Fig. 5

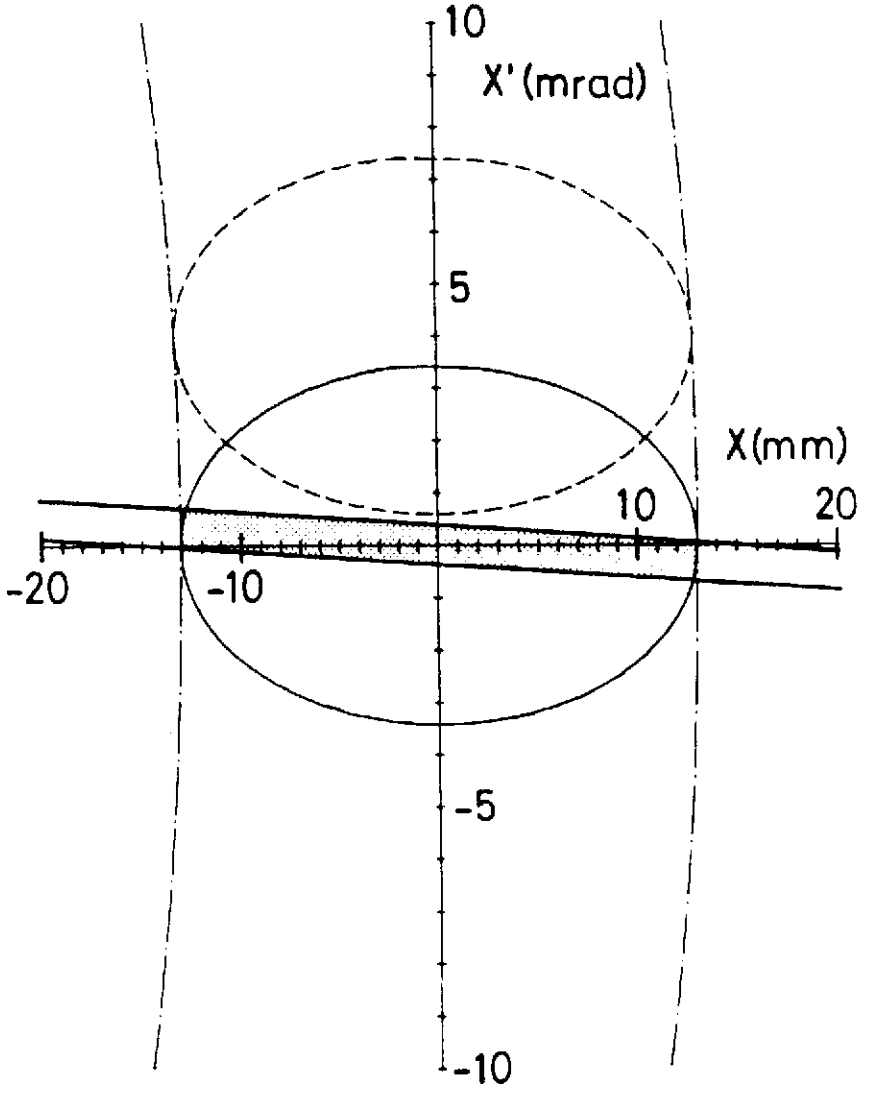
10
X' (mrad)
5
X(mm)
10
20
-20
-10
-5
-10

Fig. 7

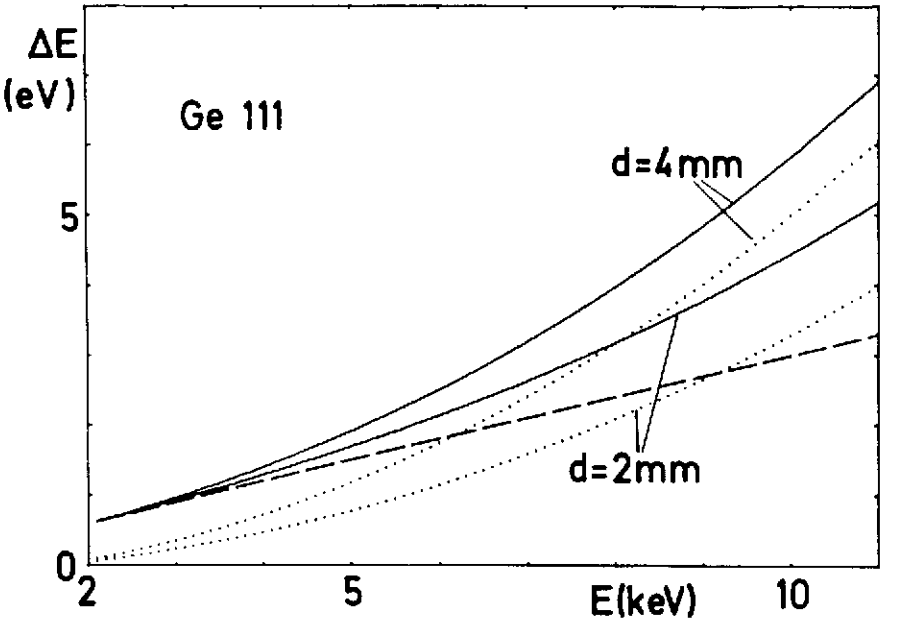
ΔE
(eV)
Ge 111
d=4mm
d=2mm
5
0
2
5
E(keV)
10

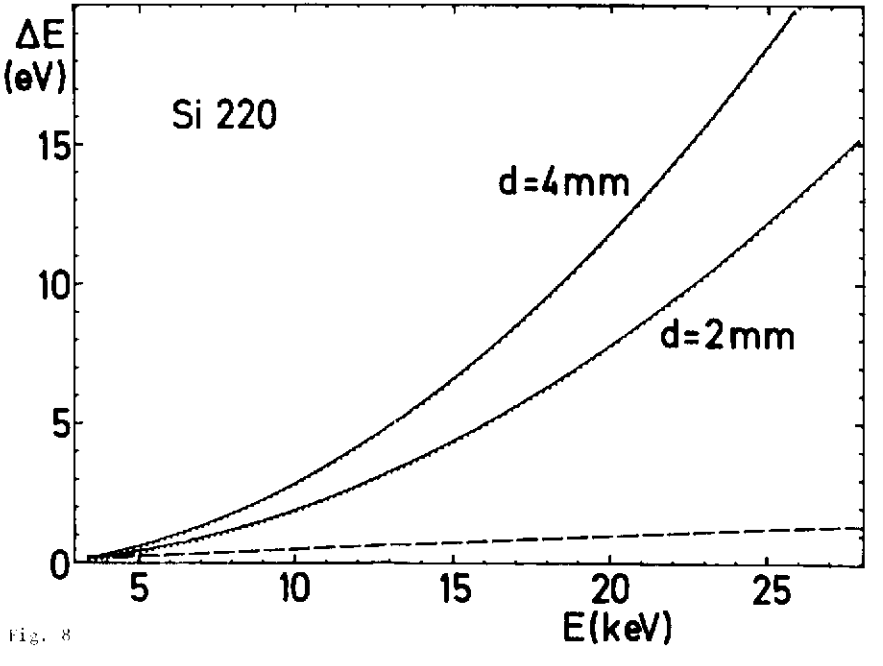
ΔE
(eV)
Si 220
d=4mm
d=2mm
15
10
5
0
5
10
15
20
25
E(keV)

Fig. 8

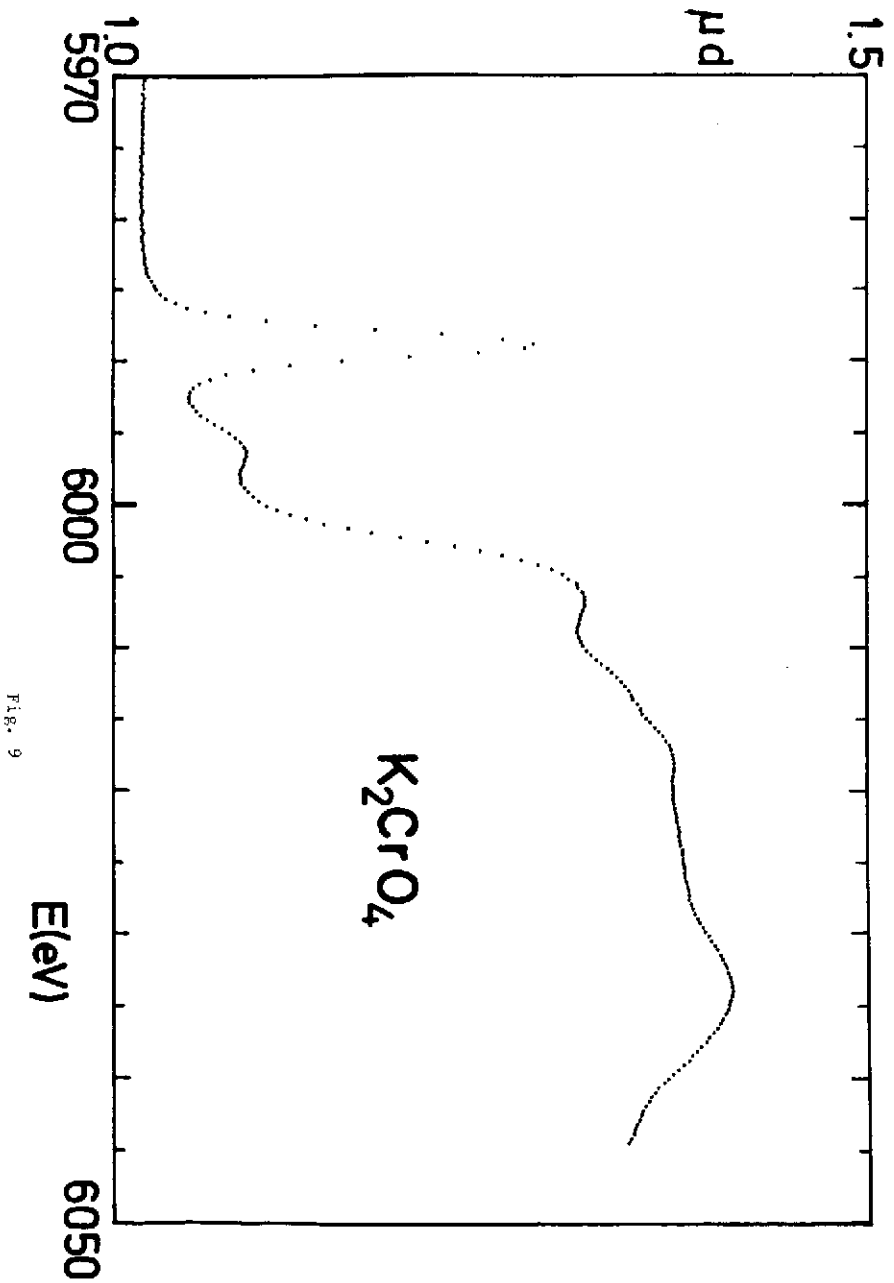
10
μd
15
5970
6000
6050
E(eV)
K_2CrO_4

Fig. 9

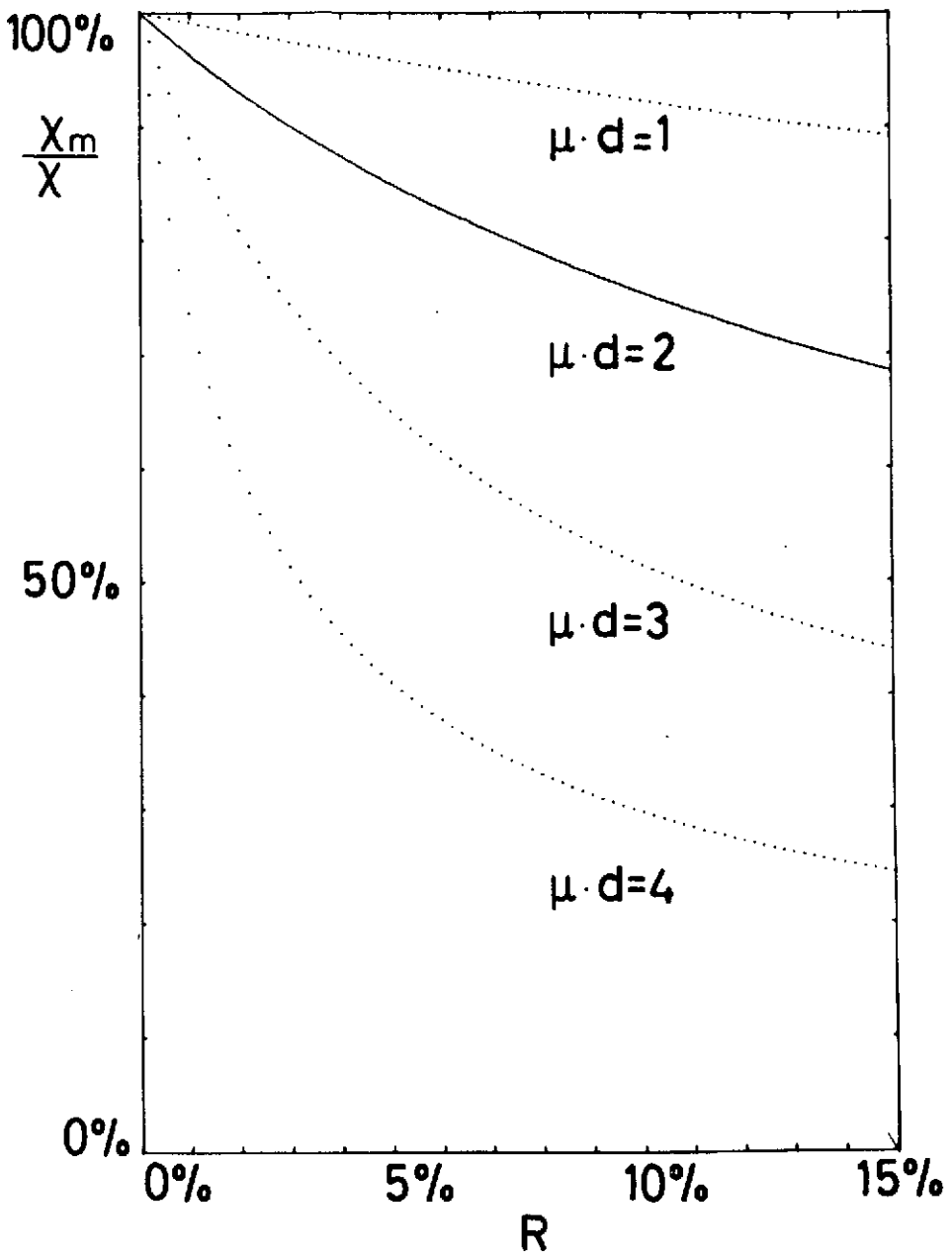
100%
$\frac{X_m}{X}$
μ·d=1
μ·d=2
μ·d=3
μ·d=4
50%
0%
0%
5%
10%
15%
R

Fig. 10